https://doi.org/10.3311/PPci.22784
Creative Commons Attribution

Periodica Polytechnica Civil Engineering, 68(2), pp. 445–458, 2024

Free Vibration of Axially Functionally Graded Timoshenko Circular Arch

Joon Kyu Lee[1], Hee Min Yoon[2], Sang Jin Oh[3], Byoung Koo Lee[4*]

[1] Department of Civil Engineering, University of Seoul, 163 Seoulsiripdae-ro, Dongdaemun-gu, Seoul 02504, Republic of Korea
[2] Saman Corporation, 13 Byeoryangsangga-ro, Gwacheon-si, Gyeonggi-do 13837, Republic of Korea
[3] Department of Civil and Environmental Engineering, Jeonnam State University, 152 Jookrokwon-ro, Damyang-eup, Damyang-gun, Jeonnam 57337, Republic of Korea
[4] Department of Civil and Environmental Engineering, Wonkwang University, 460 Iksan-daero, Iksan, Jeonbuk 54538, Republic of Korea
[*] Corresponding author, e-mail: bkleest@wku.ac.kr

Received: 12 June 2023, Accepted: 19 October 2023, Published online: 15 November 2023

Abstract

Functionally graded materials are innovative composites of hybrid ceramics and metals that exhibit excellent mechanical performance in harsh temperature environments and under various external loads. In this study, the free vibrations of Timoshenko circular arches, made of functionally graded materials in the axial direction, are investigated. The material properties of Young's modulus and mass density of the arch vary according to a symmetric quadratic function along the arch axis. Differential equations governing the free vibration of the arch including the rotatory inertia and shear deformation, called the Timoshenko arch, are derived. A novel numerical solution method is developed to calculate the natural frequencies and mode shapes of the arch. Parametric studies of the modular ratio, shear correction factor, shear modulus ratio, and slenderness ratio on the natural frequencies are conducted, and the results are reported in the tables and figures.

Keywords

free vibration, axially functionally graded material, Timoshenko arch, natural frequency, mode shape

1 Introduction

The arch is one of the most important conventional structural members because it is visually appealing and offers excellent structural performance as a compression member. In particular, arches are widely used as frame structures in many engineering fields such as civil, aerospace, and shipbuilding engineering, etc. because they can be used in wide working spaces under arch clearance [1].

The dynamic load generates a member that weakens the structure owing to the resonance condition of the free vibrations. Therefore, free vibration characteristics are an important research topic in the field of structural analysis, from the design stage of structures to the health monitoring of public facilities [2].

Functionally graded materials (FGMs) are innovative materials whose material properties, such as Young's modulus and mass density, change progressively with the dimensions [3]. In addition, FGMs have the ability to withstand harsh environmental conditions, and have the structural performance to support axial and bending loads. Because they are synthesized from hybrid materials, they possess various axial strength and bending stiffness properties [4]. FGMs have been used in almost all fields of engineering since 1984, when FGMs were conceptualized in Japan. Many papers related to FGMs have been published, especially on the structural analysis of FGMs supporting various load systems. Some typical topics dealing with various types of FGMs were introduced: FGMs with temperature-dependent properties [5]; FGMs via 2D and quasi-3D refined shear deformation theories [6]; composite sandwich structures combined with the influence of porosity [7]; and ceramic-metal FGMs in a hygrothermal environment [8, 9].

FGMs are divided into two main categories according to their grade direction: axially functionally graded material (AFGM) and laterally functionally graded material (LFGM). For the AFGM, the material properties were

Cite this article as: Lee, J. K., Yoon, H. M., Oh, S. J., Lee, B. K. "Free Vibration of Axially Functionally Graded Timoshenko Circular Arch", Periodica Polytechnica Civil Engineering, 68(2), pp. 445–458, 2024. https://doi.org/10.3311/PPci.22784

graded along the axial direction. The material properties for LFGM are graded along the lateral direction of the beam axis. In this study, the focus was mainly on AFGMs.

Considering that the focus of the study is on free vibrations of the FGM arch, the research trends of free vibrations in uniform (conventional) material and the FGM arches are reviewed. The free vibration solutions of the arch can be divided into exact and approximate solutions. The exact form solution was investigated by Tufekci and Ozdemir [10], Lü and Lü [11], and others but the result of the study is very rare because the solution is very complicated. The approximate-form solution was obtained using numerical methods to calculate the mode shape by numerically integrating the differential equations and the eigenvalue of the natural frequency using the determinant search method [12]. These include studies by Lee and Lee [12], Joo et al. [13], Huynh et al. [14], Bozyigit and Acikgoz [15], Nieh et al. [16], Malekzadeh et al. [17], Shin et al. [18], and Noori et al. [19]. Because it is important to select a proper arch shape in the design of an arched structure, various shaped arches have been investigated, such as the circular arch by Tufekci and Ozdemir [10], Lü and Lü [11], Malekzadeh et al. [17] and Shin et al. [18], parabolic arch by Joo et al. [13] and Oh et al. [20], elliptical arch by Nieh et al. [16] and Rajasekaran [21], catenary arch by Wilson and Lee [22], sinusoidal arch by Rajasekaran [21] and elastica arch by Perkins [23]. The AFGM arch considered in this study is a circular arch.

Other issues considered in literature include the variable cross-section by Tufekci and Ozdemir [10], Shin et al. [18] and by Noori et al. [19], material properties by Lü and Lü [11] and Malekzadeh et al. [17] and multi-span arches by Riedel and Kang [24], etc. As mentioned above, free vibration studies of arches are still being actively conducted owing to the various applications of arch-framed structures. Studies on AFGMs include papers on stability analysis by Nieh et al. [16] and Ranganathan et al. [25]; nonlinear behavior analysis by Horibe and Mori [4]; stability optimization by Lee and Lee [26]; foundation structure by Sofiyev [27]; mechanical response of FGM beams by Boumezbeur et al. [28]; static bending-torsion of FG cantilever beams by Guendouz et al. [29]; and bending-torsion of 1D/3D beams based on the Saint-Venant's solution and taking into account the edge effects by Guendouz et al. [30].

Another important issue to be considered in free vibration analysis is whether to include or exclude the effects of rotatory inertia and shear deformation in the theoretical analysis. Ordinary beam theory excludes both rotatory inertia and shear deformation, whereas Timoshenko beam theory includes both [31, 32]. This study focuses on the Timoshenko beam theory.

According to the Timoshenko beam theory, the displacement of structures increases; thus, the effect degrades the natural frequency [33, 34]. Many studies have dealt with the Timoshenko beam theory since 1921, when Timoshenko published his paper. Li [35] investigated a unified model for analyzing the static and dynamic behaviors of FGM Timoshenko beams. Shahba et al. [36] studied the free vibration of FGM Timoshenko beams with nonclassical boundary conditions. Huang et al. [37] analyzed the free vibration of FGM tapered Timoshenko beams. Deng et al. [38] studied the free vibration of a doubly functionally graded Timoshenko beam resting on a Winkler foundation and Şimşek [39] investigated the stability of Timoshenko beams made of two-dimensional FGMs with different boundary conditions. For the free vibration of the FGM arch, Javania et al. [32] studied arbitrarily thick FGM deep arches using the unconstrained higher-order shear deformation theory based on the Timoshenko beam theory. There are many studies dealing with free vibration of arches considering the Timoshenko beam theory, for example, the studies by Caliò et al. [40] and Kim et al. [41]. Although the literature surveyed by the authors maybe limited, there is only one paper by Javania et al. [32] on the FGM Timoshenko Arch. Studies on the free vibration of FGM arches based on Timoshenko beam theory are rare. Furthermore, the study by Javania et al. [32] was also concerned with the LFGM arch, and not the AFGM arch considered in this study.

Based on the literature reviewed, this study addresses the free vibration behavior of the AFGM Timoshenko circular arch. The differential equations governing free vibration are derived based on the Timoshenko beam theory, which involves rotatory inertia and shear deformation. The differential equations are solved numerically to compute the natural frequencies with their mode shapes. Because the arch structure must maintain the axial force and bending moment, it is desirable to include the tangential displacement due to the axial force in the arch analysis, and this study includes this tangential displacement effect.

2 Graduation of material properties of AFGM

Fig. 1 (a) represents the problem statement, considered in this study, of the free vibration of a uniform, symmetric circular arch with radius r and opening angle α. The arch

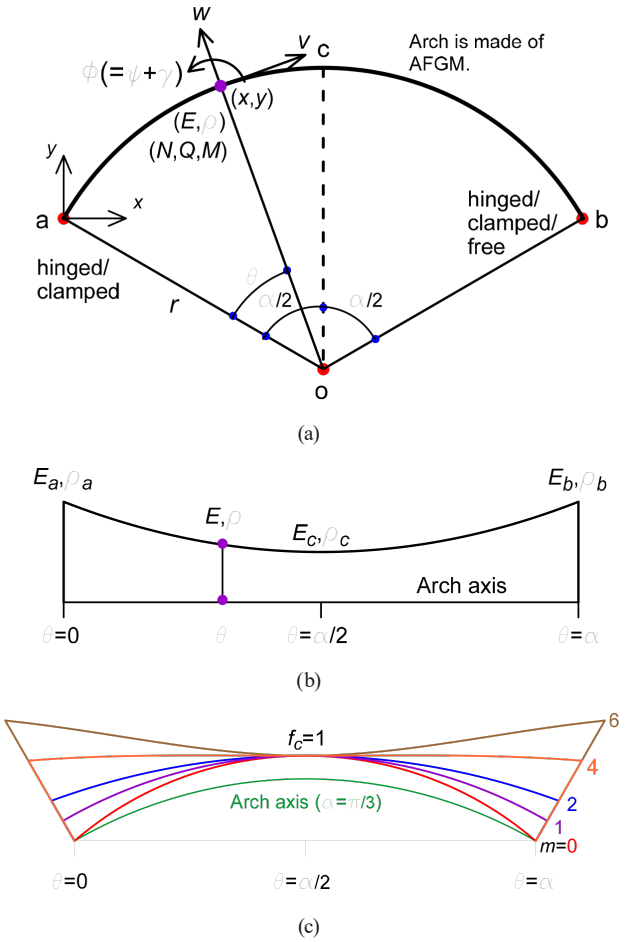

Fig. 1 (a) Problem statement of free vibration of AFGM circular arch; (b) Graded function of material properties of (E, ρ) along angular coordinate θ; and (c) Example of profile of graduation f

axis can be defined in polar coordinates (r, θ) with datum line $\overline{ao}$, or using Cartesian coordinates (x, y) with origin a. The arch is made of an axially functionally graded material. The material properties of the AFGM, namely, the Young's modulus E and mass density ρ are graded functionally along the angular coordinate θ as shown in Fig. 1 (b). The E and ρ at the left end $a(\theta = 0)$, are denoted by E_a and ρ_a, respectively, and at the arch crown $c(\theta = \alpha/2)$, $E = E_c$ and $\rho = \rho_c$. At the right end $b(\theta = \alpha)$, $E_b = E_a$ and $\rho_b = \rho_a$ because the geometry of the arch is symmetric with respect to the arch crown c.

To determine the graded function of (E, ρ) for the AFGM arches, the modular ratio m is defined as

$$m = \frac{E_a}{E_c}\left(=\frac{\rho_a}{\rho_c}\right). \tag{1}$$

In general, the graded function of (E, ρ) in Fig. 1 (b) is arbitrary. However, in this study, a quadratic function [32], which is a power-law function [42], is selected and expressed as

$$E = E_c\left[4(m-1)\left(\frac{\theta^2}{\alpha^2}-\frac{\theta}{\alpha}\right)+m\right] = E_c f,\ \ \rho = \rho_c f \tag{2}$$

for $0 \le \theta \le \alpha$,

where f is a nondimensional function of θ defined as

$$f\left(=\frac{E}{E_c}=\frac{\rho}{\rho_c}\right) = 4(m-1)\left(\frac{\theta^2}{\alpha^2}-\frac{\theta}{\alpha}\right)+m \text{ for } 0 \le \theta \le \alpha. \tag{3}$$

For example, for the profile of the graduation f in Eq. (3), its variation curves are illustrated in Fig. 1 (c) in angular coordinates, from which a suitable graduation f can be adopted by choosing m for engineering purposes.

3 Mathematical modeling of free vibration of AFGM circular arch

3.1 Governing differential equations

In the geometry of the arch shown in Fig. 1 (a), the left end a is hinged or clamped, and the right end b was hinged, clamped, or free. Thus, four types of arch-end constraints are combined: Hinged–hinged, Hinged–clamped, Clamped–clamped, and Clamped–free ends.

When the arch is under free vibration, the positive radial and tangential displacements, w and v, and the positive total rotation $\phi(=\psi+\gamma)$ of the cross-section consisting of the bending rotation ψ and shear deformation γ are shown in Fig. 1 (a) in polar coordinates (r, θ). The displacements w and v also cause stress-resultants from the axial force N, shear force Q and bending moment M at the cross-section.

As shown in Fig. 2, the small element of the vibrating arch defines the positive directions of N, Q and M, where the element of the arch has mass, resulting in a radial inertia force P_r, tangential inertia force P_t, and rotatory inertia T.

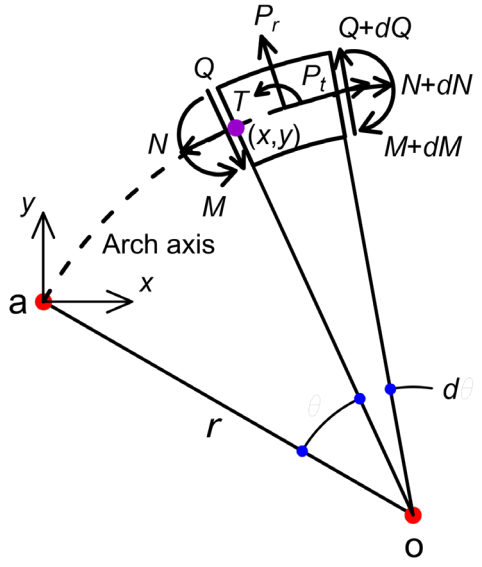

Fig. 2 Forces subjected to small arch element

The inertia forces and the rotatory inertia treated as equivalent static quantities; therefore the three equations for "dynamic equilibrium" are set as [20, 43]

$$\frac{dN}{d\theta}+Q-rP_t=0\,, \tag{4}$$

$$\frac{dQ}{d\theta}-N-rP_r=0\,, \tag{5}$$

$$\frac{1}{r}\frac{dM}{d\theta}-Q+T=0. \tag{6}$$

The total rotation of cross-section $\phi(=\psi+\gamma)$ with respect to w and v [1] is

$$\phi=\psi+\gamma=\frac{1}{r}(w'-v)\,, \tag{7}$$

from which γ can be obtained as

$$\gamma=\frac{1}{r}\left(w'-v-r\psi\right), \tag{8}$$

where $(')$ denotes the differentiation operator, that is $(') = d/d\theta$.

The equations that relate N, Q and M to w and v are [43]

$$N=\frac{EA}{r}(w+v')+\frac{EI}{r^2}\psi'=E_cf\left[\frac{A}{r}(w+v')+\frac{I}{r^2}\psi'\right], \tag{9}$$

$$Q=kAG\gamma=\frac{kAG}{r}\left(w'-v-r\psi\right), \tag{10}$$

$$M=-\frac{EI}{r}\psi'=-\frac{E_cI}{r}f\psi'\,, \tag{11}$$

where A and I are the cross-sectional area and moment of inertia of the plane area, respectively; and E and G are the Young's modulus and shear modulus, respectively. Here, E of the AFGM arch is defined as $E = E_cf$ in Eq. (2) and is substituted into Eqs. (9)–(11). In Eq. (10), k is the shear correction factor for a given cross-sectional shape. For the circular cross-section, k = 0.9 and for the square cross-section, k = 0.833 [44].

The shear modulus G for a given Poisson's ratio v is expressed as [45]

$$G=\frac{E}{2(1+v)}=\frac{E_cf}{2(1+v)}=G_cf\,, \tag{12}$$

where G_c is the shear modulus at the arch crown c.

Combining Eq. (10) and Eq. (12) yields

$$Q=\frac{kAG_c}{r}f\left(w'-v-r\psi\right). \tag{13}$$

The arch is assumed to be in harmonic motion, or each dynamic coordinate is proportional to $\sin(\omega_i t)$, for example, $w(\theta, t) = w\sin(\omega_i t)$, where ω_i is the natural frequency with the integer mode number i = 1, 2, 3, …, and t is time. The inertia loadings are then [46]:

$$P_r=-\rho A\omega_i^2w=-\rho_cA\omega_i^2fw\,, \tag{14}$$

$$P_t=-\rho A\omega_i^2v=-\rho_cA\omega_i^2fv\,, \tag{15}$$

$$T=-\rho I\omega_i^2\psi=-R_i\rho_cI\omega_i^2f\psi\,, \tag{16}$$

where ρ of the AFGM arch has already been defined as $\rho = \rho_c f$ in Eq. (2) and is substituted into Eqs. (14)–(16). In Eq. (16), R_i is the rotatory inertia index whose value is dependent on whether the rotatory inertia T is excluded or included in the theory.

$$\begin{aligned}&R_i=0 \text{ when } T \text{ is excluded,}\\ &R_i=1 \text{ when } T \text{ is included.}\end{aligned} \tag{17}$$

Differentiating Eqs. (9), (13), and Eq. (11) once gives the following derivatives:

$$\frac{dN}{d\theta}=E_cf'\left[\frac{A}{r}(w+v')+\frac{I}{r^2}\psi'\right]+E_cf\left[\frac{A}{r}(w'+v'')+\frac{I}{r^2}\psi''\right], \tag{18}$$

$$\frac{dQ}{d\theta}=\frac{kAG_c}{r}\left[f'\left(w'-v-r\psi\right)+f\left(w''-v'-r\psi'\right)\right], \tag{19}$$

$$\frac{dM}{d\theta}=-\frac{E_cI}{r}\left(f'\psi'+f\psi''\right), \tag{20}$$

where the first derivative f' is obtained from Eq. (3):

$$f'=4(m-1)\left(\frac{2\theta}{\alpha^2}-\frac{1}{\alpha}\right). \tag{21}$$

By substituting the stress-resultants N, Q, and M with their derivatives in Eqs. (4)–(6) yield

$$\begin{aligned}w''=&\frac{E_c}{kG_c}\left(w+v'+\frac{I}{Ar}\psi'\right)-\frac{f'}{f}\left(w'-v-r\psi\right)+v'+r\psi'\\&-\frac{r^2\rho_c}{kG_c}\omega_i^2w,\end{aligned} \tag{22}$$

$$\begin{aligned}v''=&-\frac{f'}{f}\left(w+v'+\frac{I}{Ar}\psi'\right)-w'-\frac{I}{Ar}\psi''\\&-\frac{kG_c}{E_c}\left(w'-v-r\psi\right)-r^2\frac{\rho_c}{E_c}\omega_i^2v,\end{aligned} \tag{23}$$

$$\psi''=-\frac{kAr^2}{I}\frac{G_c}{E_c}\left(\frac{w'}{r}-\frac{v}{r}-\psi\right)-\frac{f'}{f}\psi'-R_ir^2\frac{\rho_c}{E_c}\omega_i^2\psi. \tag{24}$$

To facilitate the numerical studies, the following dimensionless system variables are introduced:

$$\delta = \frac{w}{r}, \tag{25}$$

$$\lambda = \frac{v}{r}, \tag{26}$$

$$\mu = \frac{G_c}{E_c}\left(= \frac{1}{2(1+\nu)}\right), \tag{27}$$

$$s = \frac{r}{\sqrt{I/A}}, \tag{28}$$

$$C_i = r\omega_i\sqrt{\rho_c/E_c}, \tag{29}$$

where (δ, λ) are the normalized displacements, μ is the shear modulus ratio, s is the slenderness ratio, and C_i is the frequency parameter.

By substituting the system variables in Eqs. (25)–(29) into the dimensional form of Eqs. (22)–(24) the dimensionless differential equations that govern the free vibration of the AFGM circular arch, considering the rotatory inertia and shear deformation, are obtained as follows:

$$\delta'' = \frac{1}{k\mu}\left(\delta + \lambda' + \frac{1}{s^2}\psi'\right) - \frac{f'}{f}\left(\delta' - \lambda - \psi\right) + \lambda' + \psi' - \frac{C_i^2}{k\mu}\delta, \tag{30}$$

$$\lambda'' = -\frac{f'}{f}(\delta + \lambda') - \delta' - C_i^2\left(\lambda - \frac{R_i}{s^2}\psi\right), \tag{31}$$

$$\psi'' = -k\mu s^2\left(\delta' - \lambda - \psi\right) - \frac{f'}{f}\psi' - R_i C_i^2\psi, \tag{32}$$

where, once again, k is the shear correction factor for a given cross-sectional shape in Eq. (10), and f and f' are as defined in Eq. (3) and Eq. (20), respectively. Note that C_i is the eigenvalue of the governing differential equations to be determined using appropriate numerical solution method.

3.2 Boundary conditions

Now consider the boundary conditions. For the hinged ends (θ = 0 and θ = α), w, v, and M in Eq. (11) are zero. The dimensionless forms are expressed as follows:

$$\delta = 0,\ \lambda = 0,\ \psi' = 0. \tag{33}$$

For the clamped end (θ = 0 and θ = α), w, v, and ψ are zero, that is

$$\delta = 0,\ \lambda = 0,\ \psi = 0. \tag{34}$$

For the free end (θ = α), N, Q and M (Eqs. (9)–(11)) are zero, that is,

$$\delta + \lambda' = 0,\ \delta' - \lambda - \psi = 0,\ \psi' = 0. \tag{35}$$

3.3 Numerical solution methods

In the differential equations Eqs. (30)–(32), the arch parameters are: end constraint; opening angle α; radius of circular arch r; cross-sectional area A; moment of inertia of the plane area I; material properties (E_a, ρ_a) and (E_c, ρ_c); shear correction factor k; and Poisson's ratio v. According to these arch parameters, the modular ratio m, shear modulus ratio μ and slenderness ratio s, which are the parameters required by Eqs. (30)–(32), can be obtained. Then, a numerical integration method, such as the Runge-Kutta method [47], is used to integrate Eqs. (30)–(32) for calculating the mode shape of $(\delta, \lambda)_i$, subject to boundary conditions of Eqs. (33)–(35), based on the selected end constraint. The determinant search method combined with the Regula-Falsi method [47], which is one of the solution methods for nonlinear equations, is used to determine the eigenvalue C_i. This type of solution method for initial and boundary value problems with eigenvalues has frequently been used in the literature [21, 26, 41]. The numerical solution method is as follows:

1. Input the arch parameters of the end constraint and (m, μ, s, α, R_i, S_i).
2. Set a trial frequency C_i. The starting value of the trial frequency C_i is C_i = 0.
3. Integrate Eqs. (30)–(32) subject to the boundary conditions in Eq. (33)–(35) at θ = 0, according to the given end constraint using the Runge-Kutta method. Then, the trial deformation (δ, λ) is obtained in $0 \le \theta \le \alpha$.
4. In executing the above step, evaluate the determinant D of the boundary conditions at θ = α, using Eq. (33)–(35), and consider the following convergence criterion:

   $$|D| \le 1\times10^{-8}. \tag{36}$$

   When the criteria in Eq. (36) is satisfied, stop calculating and output C_i with (δ, λ).
5. Otherwise, increment the frequency by Δ from the value just before the trial C_i and go to Step 2 with a new forward trial frequency $C_i (\leftarrow C_i + \Delta)$.
6. Check whether the sign of $D_a \times D_b$ is negative during Steps 2–5, where D_a and D_b are D values corresponding to the previous and current trials, respectively.
7. If the sign of $D_a \times D_b$ becomes negative, the solution C_i is between $C_{i,a}$ and $C_{i,b}$. An advanced trial $C_{i,c}$ to solution C_i is calculated using the Regula-Falsi method as follows:

$$C_{i,c} = \frac{C_{i,a}|D_b| + C_{i,b}|D_a|}{|D_a| + |D_b|}. \tag{37}$$

8. Once Step 7 is completed, iterate the above steps until the following criterion is satisfied:

$$\frac{C_{i,b} - C_{i,a}}{C_{i,b}} \le 1 \times 10^{-5}. \tag{38}$$

9. When the criterion given by Eq. (38) is satisfied, stop calculating and output $C_{i,c}$ with (δ, λ).

The algorithm for the numerical solution methods developed in this study was self-coded using FORTRAN, which includes a subroutine program that calculates (E, ρ) along the arch axis, as described in Section 2.

Before running the numerical experiments, it is important to determine the step size $\Delta\theta$ in the Runge-Kutta method to efficiently integrate Eqs. (30)–(32). A convergence analysis was performed by varying the step size $\Delta\theta$, and the results are shown in Fig. 3, where the arch parameters are listed. The solutions C_1 for the four end constraints give good convergence with the number of dividing elements $\alpha/\Delta\theta$ = 10. Fig. 4 shows that, for the Hinged–hinged end, the trial solution C_1 = 0.1728 for $\alpha/\Delta\theta$ = 10 convergences sufficiently to the target solution C_1 = 0.1725 for $\alpha/\Delta\theta$ = 100 with a convergence rate of 0.998 (= 0.1725/0.1728). For further numerical calculations in this study, $\alpha/\Delta\theta$ = 50 is used, where the trial C_1 goes to C_1 = 0.1725 with 4–digit accuracy. All solutions with

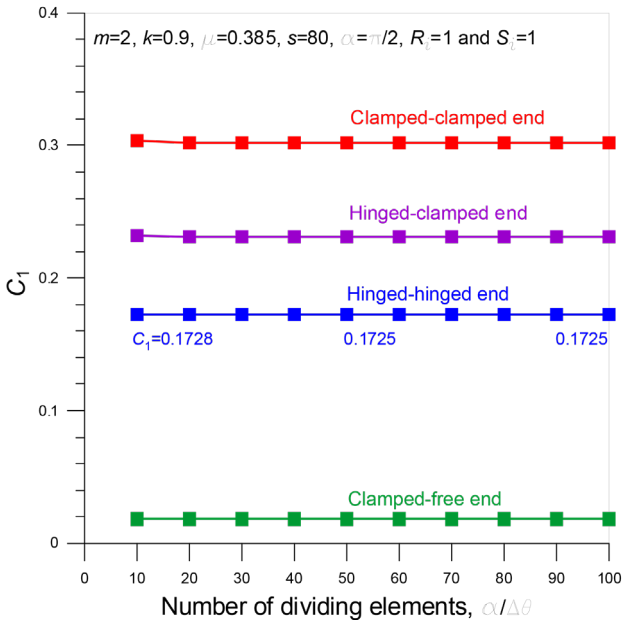

Fig. 3 Convergence analysis for Runge-Kutta method

$\alpha/\Delta\theta$ = 50 are calculated on a PC with graphics capability (Samsung DM530AFA-L78A 8GB, M.2 512GB), with a computation time of 0.03 s per problem.

4 Numerical experiments and discussion

The first numerical experiment compared the values of natural frequencies ω_i in this study with those available in literature to validate the theories and numerical methods employed in this study, and the results are listed in Table 1. The arch parameters considered are: $\alpha = \pi/2$; k = 0.9 for a circular cross-section with diameter = 0.1 m ($A = 7.854 \times 10^{-3}$ m^2 and $I = 4.909 \times 10^{-6}$ m^4); r = 2 m; v = 0.3; E_a = 70 GPa, ρ_a = 2700 kg/m^3 for pure aluminum (Al); and E_c = 140 GPa, ρ_c = 5400 kg/m^3 for the zirconia (ZrO_2). From these arch parameters, the remaining parameters are obtained as m = 2, μ = 0.385 and s = 80. The values of C_i calculated by solving Eq. (30) and Eq. (32) are converted into ω_i = 2545.9 C_i rad/s using Eq. (29). For the finite element method (FEM) solutions, ADINA software was chosen, where the AFGM arch was modeled as 50 stepped-beam elements with varying material properties (E, ρ) according to Eq. (2). In Table 1, for the first three natural frequencies of $\omega_{i=1,2,3}$ in rad/s, the two results are in good agreement, with an average error of 0.47%, and a maximum error of 0.82%. The results validate the theoretical and numerical methods developed in this study.

Now a parametric study of the arch parameters (k, m, μ, s, α, R_i, S_i) with end constraints on the frequency parameters $C_{i=1,2,3}$ and mode shape $(\delta, \lambda)_i$ is performed and results are reported in Tables 2–5 and Figs. 4–7.

Table 2 illustrates the effects of the end constraint on $C_{i=1,2,3}$. The arch parameters are listed in Table 2. Irrespective of mode i, the largest and smallest C_i values were achieved for the Clamped–clamped and Clamped–free ends, respectively. The value of C_i varies significantly depending on the end constraint. For C_i, that is, i = 1, C_i at the Clamped–clamped end is 9.48 times greater than C_i at the Clamped–free end. It is clear that a greater fixation of the end constraint of the arch provides higher frequencies. For example, C_i at the Clamped–clamped end is greater than C_i at the Clamped–hinged end, even though the left ends of the two arches are equal to the clamped end. Therefore, it can be concluded that the end constraint is one of the most important parameters for determining the natural frequency.

The influence of the rotatory inertia T on C_i for the Hinged–clamped end is presented in Table 3 along with that of the slenderness ratio s. The remaining parameters

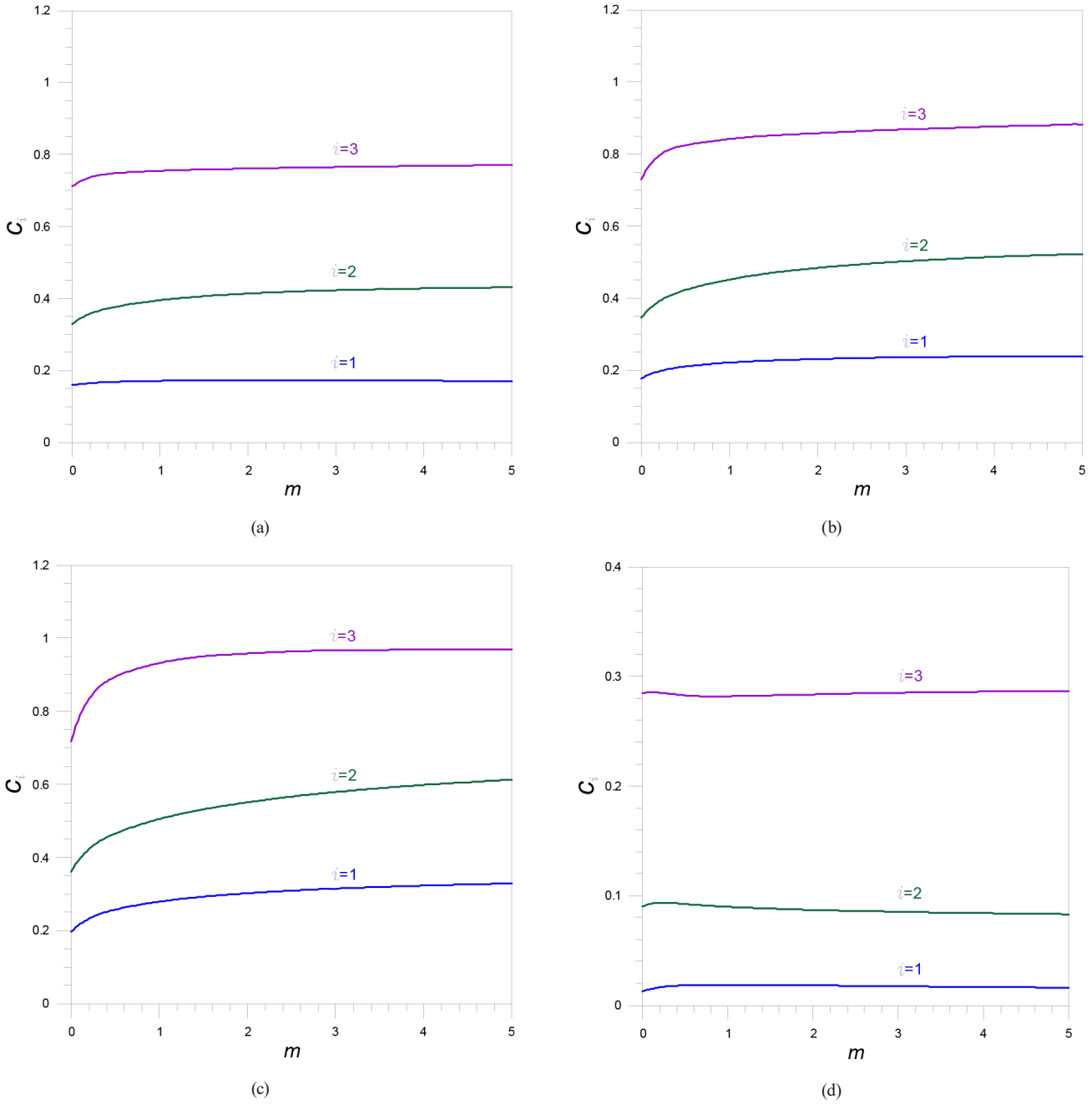

Fig. 4 Frequency curves of C_i as function of modular ratio m: (a) Hinged–hinged; (b) Hinged–clamped; (c) Clamped–clamped; and (d) Clamped–free end for $k = 0.9$, $\mu = 0.385$, $s = 80$, $\alpha = \pi/2$, $R_i = 1$ and $S_i = 1$

are listed in Table 3. If T is included in the theory ($R_i = 1$), C_i decreases. This is because T increases the structural displacement; consequently, the natural frequency decreases when T is included. The percentage difference for $i = 3$ was the least at 0.114% and the highest at 0.676%. In addition, the effect of T was more prominent for smaller s. For example, for $i = 1$, the effect of T for $s = 40$ was 5.17 (= 0.445/0.086) times greater than that of T for $s = 80$.

Table 4 shows the effect of shear deformation γ on C_i for the Hinged–clamped end with slenderness ratio s. The arch parameters are the same as in Table 3 except $\mu = \infty$ when $S_i = 0$. For $\mu = \infty$, $\gamma = 0$, which means that the effect of γ is excluded, that is, $S_i = 0$ [39]. Therefore, the value of μ for $S_i = 0$ becomes $\mu = \infty$, whereas the value of μ for $S_i = 1$ remains constant at $\mu = 0.385$. Including γ in the theory, that is $S_i = 1$, suppresses C_i. This is because γ represents the increasing effect on structural displacements, so when γ is included, the natural frequency decreases as a result. The percentage difference for $i = 3$ has the lowest value of 1.090%, and the largest value of 2.532%. The effect of γ is more dominant for smaller s. For example, for $i = 1$, the effect of γ at $s = 40$ is 3.62 (= 0.934/0.258) times greater than that at $s = 160$.

Table 1 Comparison* of natural frequency ω_i between this study and FEM

End constraint	Data source	Natural frequency ω_i (rad/s)		
		$i = 1$	$i = 2$	$i = 3$
Hinged–hinged	This study	439.10	1053.75	1938.06
	FEM	437.68	1049.68	1926.69
Hinged–clamped	This study	589.06	1232.83	2185.39
	FEM	587.23	1228.24	2192.71
Clamped–clamped	This study	769.34	1403.27	2441.19
	FEM	765.66	1409.61	2453.90
Clamped–free	This study	46.31	221.49	722.14
	FEM	46.08	222.88	728.06

* See the text for arch parameters.

Table 2 Effect* of end constraint on frequency parameter C_i

End constraint	Frequency parameter C_i		
	$i = 1$	$i = 2$	$i = 3$
Hinged–hinged	0.1725	0.4139	0.7612
Hinged–clamped	0.2314	0.4842	0.8584
Clamped–clamped	0.3022	0.5512	0.9589
Clamped–free	0.0182	0.0870	0.2836

* Arch parameters: $m = 2$; $k = 0.9$; $\mu = 0.385$; $s = 80$; $\alpha = \pi/2$; $R_i = 1$; and $S_i = 1$.

Table 3 Effect of rotatory inertia index R_i on frequency parameter C_i*

s	Index R_i	Frequency parameter C_i		
		$i = 1$	$i = 2$	$i = 3$
40	0	0.4518	0.8340	1.1016
	1	0.4498	0.8303	1.0942
	Devi. (%)**	0.445	0.446	0.676
80	0	0.2316	0.4854	0.8622
	1	0.2314	0.4842	0.8584
	Devi. (%)	0.086	0.247	0.443
120	0	0.1551	0.3287	0.5849
	1	0.1551	0.3283	0.5837
	Devi. (%)	0.	0.122	0.206
160	0	0.1165	0.2478	0.4407
	1	0.1165	0.2476	0.4402
	Devi. (%)	0.	0.081	0.114

* Arch parameters: Hinged–clamped end, $m = 2$; $k = 0.9$; $\mu = 0.385$; $\alpha = \pi/2$; and $S_i = 1$.
** Deviation $(\%) = \left(C_{i,R_i=0}/C_{i,R_i=1} - 1\right) \times 100$

Particularly at smaller s and higher i, the effect of γ should not be excluded. According to the Timoshenko beam theory, the indices are $R_i = 1$ and $S_i = 1$ so, C_i with $S_i = 1$ in Table 4 represents the Timoshenko beam theory.

Table 5 lists the effects of the shear correction factor k on C_i. The value of k depends on the cross-sectional shape. In this study, the effect of k is shown by selecting circular and square cross-sections, which are among

Table 4 Effect of shear deformation index S_i on frequency parameter C_i*

s	Index S_i	Frequency parameter C_i		
		$i = 1$	$i = 2$	$i = 3$
40	0	0.4540	0.8443	1.1219
	1	0.4498	0.8303	1.0942
	Devi. (%)**	0.934	1.686	2.532
80	0	0.2329	0.4899	0.8761
	1	0.2314	0.4842	0.8584
	Devi. (%)	0.648	1.177	2.062
120	0	0.1556	0.3303	0.5922
	1	0.1551	0.3283	0.5837
	Devi. (%)	0.322	0.609	1.456
160	0	0.1168	0.2487	0.4450
	1	0.1165	0.2476	0.4402
	Devi. (%)	0.258	0.444	1.090

* Arch parameters are the same as in Table 3 except $\mu = \infty$ for $S_i = 0$.
** Deviation $(\%) = \left(C_{i,S_i=0}/C_{i,S_i=1} - 1\right) \times 100$

Table 5 Effect of shear correction factor k on frequency parameter C_i*

End constraint	Sectional Shape	Factor k	Frequency parameter C_i		
			$i = 1$	$i = 2$	$i = 3$
Hinged–hinged	Circular	0.9	0.1725	0.4139	0.7612
	Square	0.833	0.1764	0.4229	0.7774
Hinged–clamped	Circular	0.9	0.2314	0.4842	0.8584
	Square	0.833	0.2365	0.4943	0.8747
Clamped–clamped	Circular	0.9	0.3022	0.5512	0.9589
	Square	0.833	0.3088	0.5616	0.9621
Clamped–free	Circular	0.9	0.0182	0.0870	0.2836
	Square	0.833	0.0186	0.0890	0.2899

* See the text for arch parameters.

the most practical cross-sections for arch structures. Here, $k = 0.9$ and $k = 0.833$ for the circular and square cross-sections, respectively [38]. The value of C_i for the square cross-section was always greater than that for the circular cross-section. This implies that C_i for a smaller k is greater than that for a larger k. In Table 5, C_i for square cross-sections is on average approximately 2% greater than for circular cross-sections.

The frequency curve of C_i as a function of modular ratio m is shown in Fig. 4. The remaining parameters are: $k = 0.9$; $\mu = 0.385$; $s = 80$; $\alpha = \pi/2$; $R_i = 1$; and $S_i = 1$. In general, C_i tended to increase with m. The rate of increase is very moderate, and for $m > 2$, the effect of m is almost negligible because the frequency curve converges to a horizontal asymptote.

The frequency curve of C_i as a function of the slenderness ratio s is shown in Fig. 5. The remaining parameters are: $m = 2$; $k = 0.9$; $\mu = 0.385$; $\alpha = \pi/2$; $R_i = 1$; and

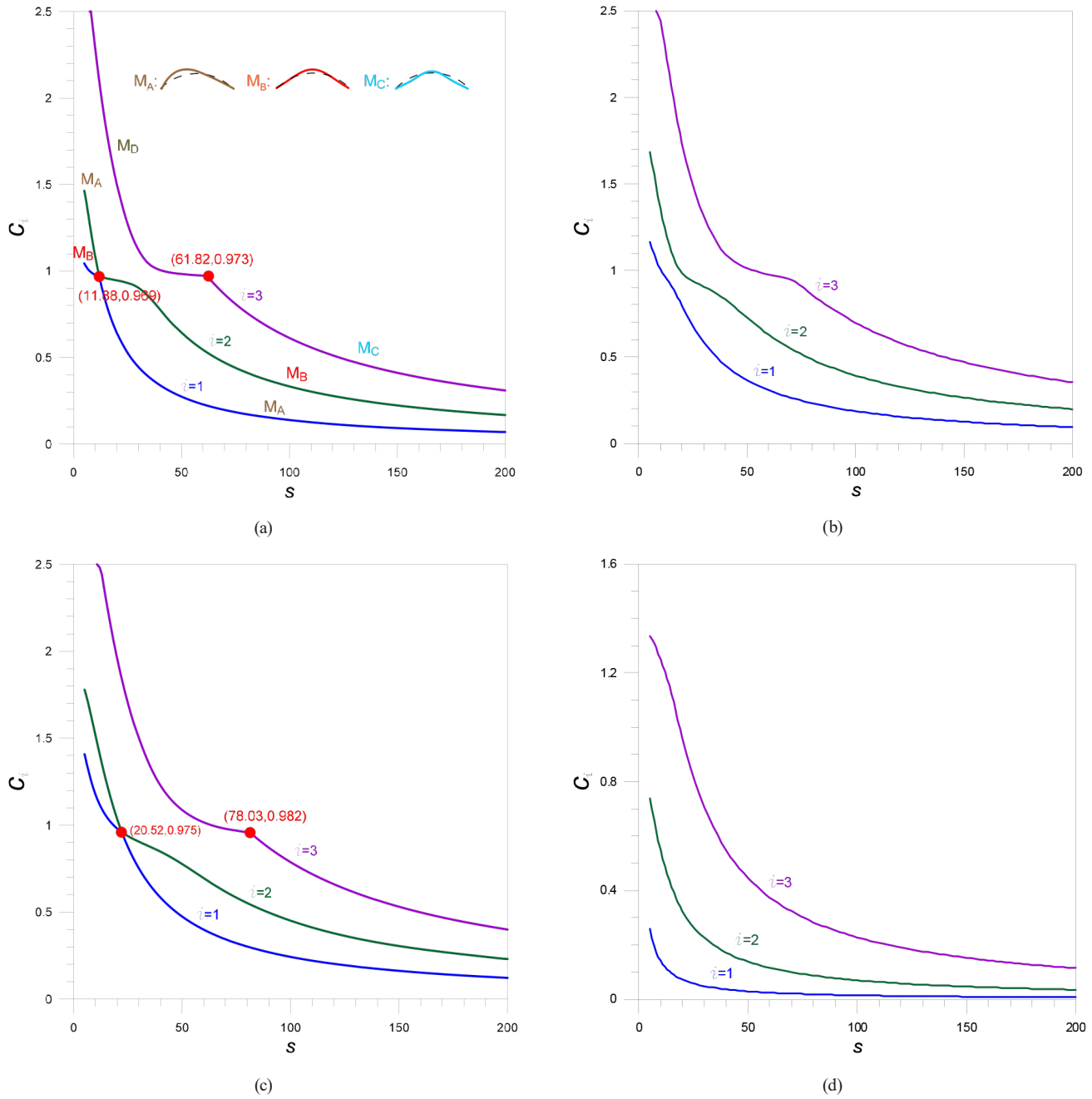

Fig. 5 Frequency curves of C_i as function of the slenderness ratio s: (a) Hinged–hinged; (b) Hinged–clamped; (c) Clamped–clamped; and (d) Clamped–free end for $m = 2$, $k = 0.9$, $\mu = 0.385$, $\alpha = \pi/2$, $R_i = 1$ and $S_i = 1$

$S_i = 1$. C_i decreases as s increases. For a smaller s, that is, approximately $s < 50$, the rate of decrease is relatively higher than at $s > 50$ and its effect is prominent. When s is small, $s < 50$, the reduction rate is relatively higher than at $s > 50$, and its effect is significant. In Fig. 5 (a) and Fig. 5 (c), for the Hinged–hinged and Clamped–clamped ends, respectively, the two frequency curves intersect such that a double root exists at a single coordinate marked with a red dot, and two mode shapes are possible at a single frequency. For example, the Hinged–hinged end in Fig. 5 (a) has a double root such that $C_1 = C_2 = 0.969$ at $s = 11.88$. The two different types of mode shape change before and after this double root indicated by red dots. For example, in Fig. 5 (a), when $s < 11.88$, the mode shape for $i = 1$ is M_B and for $i = 2$, it is M_A. The two mode shapes M_A and M_B are shown in Fig. 5 (a). However, when $s > 11.88$, the mode shape changes from M_A for $i = 1$ to M_B for $i = 2$. Similarly, at coordinates (61.82, 0.973) marked with a red dot, two frequency curves of $i = 3$ and $i = 4$ have a double root. In Fig. 5 (a), the mode shape of the M_A is anti-symmetric, whereas the mode shapes of the M_B and M_C are symmetric. Thus, for the first mode, $i = 1$, before $s = 11.88$, the mode

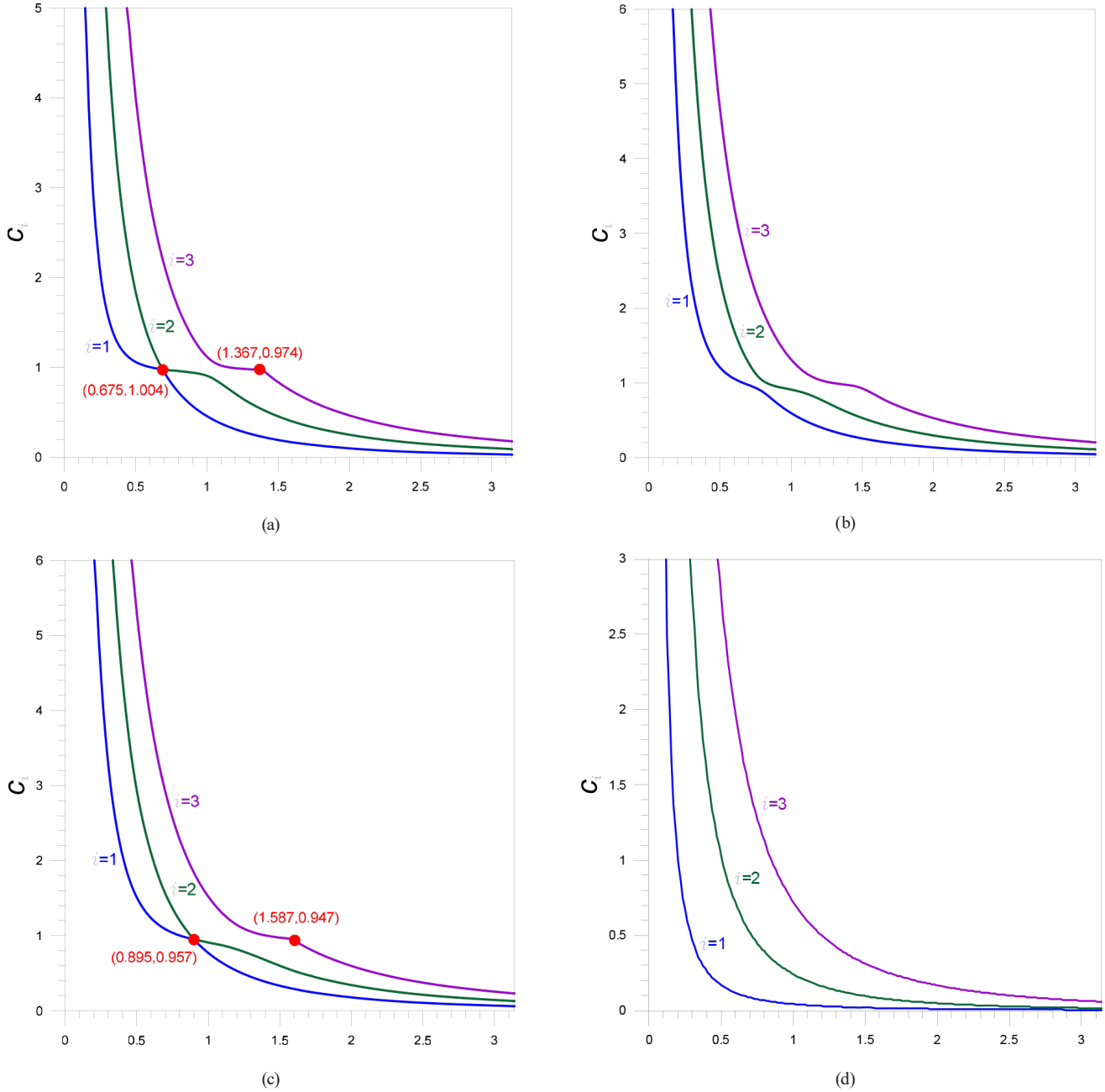

Fig. 6 Frequency curves of C_i as function of the opening angle α: (a) Hinged–hinged; (b) Hinged–clamped; (c) Clamped–clamped; and (d) Clamped–free end for $m = 2$, $k = 0.9$, $\mu = 0.385$, $s = 80$, $R_i = 1$ and $S_i = 1$

shape is symmetric (M_B), and after $s = 11.88$, the mode shape is anti-symmetric (M_A). Similarly, at $s = 61.82$, the mode shape for $i = 3$ changes from type of M_D (not shown) to the symmetric mode shape of M_C. As shown in Fig. 5 (b), the frequency curve of the Hinged–clamped end constraint approaches but does not intersect, exhibiting the so-called veering phenomenon [48].

Fig. 6 shows the frequency curve of C_i as a function of the opening angle α. The remaining parameters are: $m = 2$; $k = 0.9$; $\mu = 0.385$; $s = 80$; $R_i = 1$ and $S_i = 1$. C_i decreases as α increase. For small α, the reduction rate is relatively higher, and its effect is more significant than for large α. In Fig. 6 (a) and Fig. 6 (c) for the Hinged–hinged and Clamped–clamped end, respectively, the double roots indicated by the red dot exist as in Fig. 5 (a) and Fig. 5 (c). For the Hinged–clamped end in Fig. 6 (b), a veering phenomenon does not exist, as shown in Fig. 5 (b).

Fig. 7 (a) shows the detailed mode shapes of M_A, M_B and M_C displayed already in Fig. 5 (a). Also, Fig. 7 illustrates typical first three mode shapes of $(\xi_m, \eta_m)_i$ at Cartesian coordinates (ξ, η) corresponding to $C_{i=1,2,3}$, and the arch parameters are listed. The coordinates (ξ, η) of

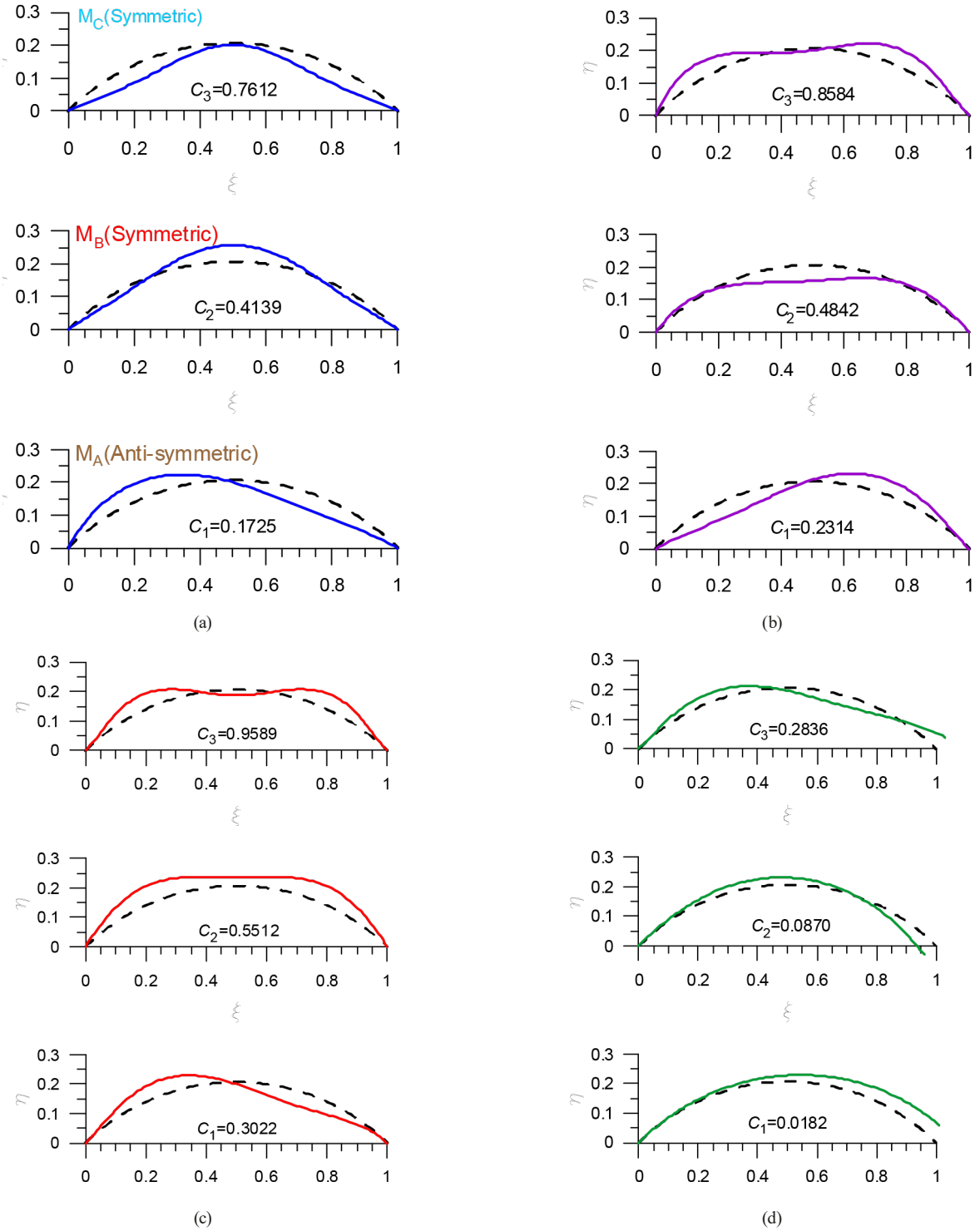

Fig. 7 First three mode shapes: (a) Hinged–hinged; (b) Hinged–clamped; (c) Clamped–clamped; and (d) Clamped–free end for $m = 2$, $k = 0.9$, $\mu = 0.385$, $\alpha = \pi/2$, $R_i = 1$ and $S_i = 1$

the undeformed arch axis, normalized by the span length $l = 2r\sin(\alpha/2)$, are expressed as

$$\xi = \frac{x}{l} = \frac{\cos t_2 - \sin t_3}{\tan t_1}, \quad \eta = \frac{y}{l} = \cos t_2 - \sin t_3, \tag{39}$$

where $t_1 = (\alpha - \theta)/2$, $t_2 = \alpha/2 - \theta$, and $t_3 = (\pi - \alpha)/2$.

From the undeformed arch axis (ξ, η) in Eq. (39), the deformed arch axis (ξ_m, η_m), i.e. mode shape of vibrating arch, is computed by combining (δ, λ) as

$$\xi_m = \xi + \lambda\cos t_2 - \delta\cos t_4, \quad \eta_m = \eta + \lambda\sin t_2 + \delta\sin t_4, \tag{40}$$

where $t_4 = (\pi - \alpha)/2 + \theta$.

The typical mode shapes $(\xi_m,\ \eta_m)_i$ corresponding to $C_{i=1,2,3}$ are shown in Fig. 7 where the arch parameters are listed. The boundary conditions expressed in Eqs. (33)–(35) are well implemented in $(\xi_m, \eta_m)_i$ at the left and right ends. To avoid resonance due to external dynamic excitation by mechanical devices, this type of mode shape provides particularly useful data in arch design, representing the relative amplitude, position of maximum amplitude, and position of the nodal point. The types of mode shape of M_A (Anti-symmetric), M_B (Symmetric) and M_C (Symmetric) already shown in Fig. 5 (a) are additionally presented in Fig. 7 (a) for reader's convenience. In Fig. 7 (b) and Fig. 7 (d), the mode shapes are neither symmetric nor anti-symmetric because the end constraint is not symmetric.

5 Conclusions

In this study, the free vibration of an axially functionally graded Timoshenko circular arch is investigated. The arch cross-section is uniform. The arch is supported at the left end by a hinged or clamped end and at the right end by a hinged or clamped or free end.

In the first part of this paper, material properties of the Young's modulus and mass density of the AFGM arch are defined as symmetric quadratic functions along the arch axis using the modular ratio.

In the second part of the study, the differential equations governing the free vibration of the AFGM circular arch are derived based on the dynamic equilibrium equations of the small arch element in harmonic motion in the free vibration state. In addition, relevant boundary conditions for the hinged, clamped, and free ends are derived. In the governing differential equations, the influences of rotatory inertia and shear deformation for the Timoshenko arche, which have an important effect on the natural frequencies, are considered.

In the third part of this study, numerical methods for solving differential equations are developed. To integrate the differential equations, the Runge-Kutta method, a direct integration method, is used, and to calculate the natural frequency as an eigenvalue of the differential equations, the Regula-Falsi method, which is a numerical method for nonlinear equations, is used. A convergence analysis of the Runge-Kutta method is performed to efficiently integrate the differential equations.

Finally parametric studies on the natural frequencies are conducted. The natural frequencies obtained in this study and the FEM solutions are in good agreement. The results of the parametric studies of the end constraint, modular ratio, shear correction factor, shear modulus ratio, slenderness ratio, and opening angle on the natural frequencies are reported in the tables and figures. The first three typical mode shapes of an AFGM arch with four end constraints are illustrated in Cartesian coordinates.

Finally, the concluding remarks summarizes the contents of the paper.

In the future, it will be necessary to study the free vibration of the arch by considering the rotatory inertia and shear deformation, which allows variable curvature and cross-section for functionally graded materials in the axial and lateral directions.

Acknowledgements

This work was supported by the 2023 Research Fund of the University of Seoul. Professor J. K. Lee is grateful for this financial support.

Declaration of conflict of interest

The authors declare that they have not any conflict of interest.

References

[1] Henrych, J. "The dynamics of arches and frames", Elsevier, 1981. ISBN 978-0444997920

[2] Rao, S. S. "Vibration of Continuous System", John Wiley & Sons, 2007. ISBN 9780471771715

[3] Zhang, N., Khan, T., Guo, H., Shi, S., Zhong, W., Zhang, W. "Functionally graded materials: An overview of stability, buckling, and free vibration analysis", Advances in Materials Sciences and Engineering, 2019, 1354150, 2019. https://doi.org/10.1155/2019/1354150

[4] Horibe, T., Mori, K. "Large deflections of tapered cantilever beams made of axially functionally graded materials", Mechanical Engineering Journal, 5(1), 17-00268, 2018. https://doi.org/10.1299/mej.17-00268

[5] Tounsi, A., Mostefa, A. H., Attia, A., Bousahla, A. A., Bourada, F., Tounsi, A., Al-Osta, M. A. "Free vibration investigation of functionally graded plates with temperature-dependent properties resting on a viscoelastic foundation", Structural Engineering and Mechanics, 86(1), pp. 1–16, 2023. https://doi.org/10.12989/sem.2023.86.1.001

[6] Amar, L. H. H., Bourada, F., Bousahla, A. A., Tounsi, A., Benrahou, K. H., Albalawi, H., Tounsi, A. "Buckling analysis of FG plates via 2D and quasi-3D refined shear deformation theories", Structural Engineering and Mechanics, 85 (6), pp. 765–780, 2023. https://doi.org/10.12989/sem.2023.85.6.765

[7] Hadji, M., Bouhadra, A., Mamen, B., Menasria, A., Bousahla, A. A., Bourada, F., Bourada, M., Benrahou, A. A., Tounsi, A. "Combined influence of porosity and elastic foundation parameters on the bending behavior of advanced sandwich structures", Steel and Composite Structures, 46(1), pp. 1–13, 2023. https://doi.org/10.12989/scs.2023.46.1.001

[8] Zaitoun, M. W., Chikh, A., Tounsi, A., Al-Osta, M. A., Sharif, A., Al-Dulaijan, S. U., Al-Zahrani, M. M. "Influence of the visco-Pasternak foundation parameters on the buckling behavior of a sandwich functional graded ceramic-metal plate in a hygrothermal environment", Thin-Walled Structures, 170, 108549, 2022. https://doi.org/10.1016/j.tws.2021.108549

[9] Al-Osta, M. A., Saidi, H., Tounsi, A., Al-Dulaijan, S. U., Al-Zahrani, M. M., Sharif, A., Tounsi, A. "Influence of porosity on the hygro-thermo-mechanical bending response of an AFG ceramic-metal plates using an integral plate model", Smart Structures and Systems, 28(4), pp. 499–513, 2021. https://doi.org/10.12989/sss.2021.28.4.499

[10] Tufekci, E., Ozdemir, O. "Exact solution of free in-plane vibration of a stepped circular arch", Journal of Sound and Vibration, 295(3–5), pp. 725–738, 2006. https://doi.org/10.1016/j.jsv.2006.01.048

[11] Lü, Q., Lü, C. F. "Exact two-dimensional solutions for in-plane natural frequencies of laminated circular arches", Journal of Sound and Vibrations, 318(4–5), pp. 982–920, 2008. https://doi.org/10.1016/j.jsv.2008.05.011

[12] Lee, J. K., Lee, B. K. "Free vibration and buckling of tapered columns made of axially functionally graded materials", Applied Mathematical Modelling, 75, pp. 73–87, 2019. https://doi.org/10.1016/j.apm.2019.05.010

[13] Joo, S. M., Park, K. K., Lee, B. K., Hwang, H. J. "Free vibration analysis of fixed ended parabolic arches", Korean Society of Civil Engineers, 5(3), pp. 31–38, 1985.

[14] Huynh, T.-A., Luu, A.-T., Lee, J. "Bending, buckling and free vibration analyses of functionally graded curved beams with variable curvatures using isogeometric approach", Meccanica, 52(11–12), pp. 2527–2546, 2017. https://doi.org/10.1007/s11012-016-0603-z

[15] Bozyigit, B., Acikgoz, S. "Determination of free vibration properties of masonry arch bridges using the dynamic stiffness method", Engineering Structures, 250, 113417, 2022. https://doi.org/10.1016/j.engstruct.2021.113417

[16] Nieh, K. Y., Huang, C. S., Tseng, Y. P. "An analytical solution for in-plane free vibration and stability of loaded elliptic arches", Computers & Structures, 81(13), pp. 1311–1327, 2003. https://doi.org/10.1016/S0045-7949(03)00057-9

[17] Malekzadeh, P., Setoodeh, A. R., Barmshouri, E. "A hybrid layerwise and differential quadrature method for in-plane free vibration of laminated thick circular arches", Journal of Sound and Vibration, 315(1–2), pp. 212–225, 2008. https://doi.org/10.1016/j.jsv.2008.02.005

[18] Shin, Y.-J., Kwon, K.-M., Yun, J.-H. "Vibration analysis of a circular arch with variable cross-section using differential transformation and generalized differential quadrature", Journal of Sound and Vibration, 309(1–2), pp. 9–19, 2008. https://doi.org/10.1016/j.jsv.2006.08.020

[19] Noori, A. R., Aslan, T. A., Temel, B. "An efficient approach for in-plane free and forced vibrations of axially functionally graded parabolic arches with nonuniform cross-section", Composite Structures, 200, pp. 701–710, 2018. https://doi.org/10.1016/j.compstruct.2018.05.077

[20] Oh, S. J., Lee, B. K., Lee, I. W. "Natural frequencies of non-circular arches with rotatory inertia and shear deformation", Journal of Sound and Vibration, 219(1), pp. 23–33, 1999. https://doi.org/10.1006/jsvi.1998.1822

[21] Rajasekaran, S. "Free vibration of tapered arches made of axially functionally graded materials", Structural Engineering Mechanics, 45(4), pp. 569–594, 2013. https://doi.org/10.12989/sem.2013.45.4.569

[22] Wilson, J. F., Lee, B. K. "In-plane free vibrations of catenary arches with unsymmetric axes", Structural Engineering and Mechanics, 3(5), pp. 511–525, 1995. https://doi.org/10.12989/sem.1995.3.5.511

[23] Perkins, N. C. "Planar vibration of an elastica arch: Theory and Experiment", Journal of Vibration and Acoustics, 112(3), pp. 374–379, 1990. https://doi.org/10.1115/1.2930518

[24] Riedel, C. H., Kang, B. S. "Free vibration of elastically coupled dual-span curved beams", Journal of Sound and Vibration, 290(3–5), pp. 820–838, 2006. https://doi.org/10.1016/j.jsv.2005.04.016

[25] Ranganathan, S. I., Abed, F. H., Aldadah, M. G. "Buckling of slender columns with functionally graded microstructures", Mechanics of Advanced Materials and Structures, 23(11), pp. 1360–1367, 2016. https://doi.org/10.1080/15376494.2015.1086452

[26] Lee, J. K., Lee, B. K. "Buckling optimization of axially functionally graded columns having constant volume", Engineering Optimization, 54(2), pp. 269–285, 2022. https://doi.org/10.1080/0305215X.2020.1862824

[27] Sofiyev, A. H. "The buckling of FGM truncated conical shells subjected to axial compressive load and resting on Winkler-Pasternak foundations", International Journal of Pressure Vessels and Piping, 87(12), pp. 753–761, 2010. https://doi.org/10.1016/j.ijpvp.2010.08.012

[28] Boumezbeur, K., Khebizi, M., Guenfoud, M. "Finite element modeling of static and cyclic response of functionality graded material beams", Asian Journal of Civil Engineering, 24(2), pp. 579–591, 2023. https://doi.org/10.1007/s42107-022-00519-8

[29] Guendouz, I., Khebizi, M., Guenfoud, H., Guenfoud, M. "Analysis of FGM Cantilever Beams under Bending-torsional Behavior Using a Refined 1D Beam Theory", Periodica Polytechnica Civil Engineering, 66(4), pp. 1262–1277, 2022. https://doi.org/10.3311/PPci.20595

[30] Guendouz, I., Khebizi, M., Guenfoud, H., Guenfoud, M., El Fatmi, R. "Analysis of torsional-bending FGM beam by 3D Saint-Venant refined beam theory", Structural Engineering and Mechanics, 84(3), pp. 423–435, 2022. https://doi.org/10.12989/sem.2022.84.3.423

[31] Timoshenko, S. P. "LXVI. On the correction for shear of the differential equation for transverse vibrations of prismatic bars", The London, Edinburgh, and Dublin Philosophical Magazine and Journal of Science, 41(245), pp. 744–746, 1921. https://doi.org/10.1080/14786442108636264

[32] Javania, M., Kianib, Y., Eslamia, M. R. "Free vibration of arbitrary thick FGM deep arches using unconstrained higher-order shear deformation theory", Thin-Walled Structures, 136, pp. 258–266, 2019. https://doi.org/10.1016/j.tws.2018.12.020

[33] Chopra, A. K. "Dynamics of structures: Theory and Applications to Earthquake Engineering", Prentice Hall, 1995. ISBN 9780138552145

[34] Lee, B. K., Oh, S. J., Lee, T. E., Kim, G. S. "Free vibrations of tapered shear deformable column", Engineering Solid Mechanics, 9(1), pp. 1–12, 2021. http://doi.org/10.5267/j.esm.2020.8.001

[35] Li, X.-F. "A unified approach for analyzing static and dynamic behaviors of functionally graded Timoshenko and Euler-Bernoulli beams", Journal of Sound and Vibration, 318(4–5), pp. 1210–1229, 2008. https://doi.org/10.1016/j.jsv.2008.04.056

[36] Shahba, A., Attarnejad, R., Marvi, M. T., Hajilar, S. "Free vibration and stability analysis of axially functionally graded tapered Timoshenko beams with classical and non-classical boundary conditions", Composites Part B: Engineering, 42(4), pp. 801–808, 2011. https://doi.org/10.1016/j.compositesb.2011.01.017

[37] Huang, Y., Yang, L.-E., Luo, Q.-Z. "Free vibration of axially functionally graded Timoshenko beams with non-uniform cross-section", Composites Part B: Engineering, 45(1), pp. 1493–1498, 2013. https://doi.org/10.1016/j.compositesb.2012.09.015

[38] Deng, H., Chen, K., Cheng, W., Zhao, S. "Vibration and buckling analysis of double-functionally graded Timoshenko beam system on Winkler-Pasternak elastic foundation", Composite Structures, 160, pp. 152–168, 2017. https://doi.org/10.1016/j.compstruct.2016.10.027

[39] Şimşek, M. "Buckling of Timoshenko beams composed of two-dimensional functionally graded material (2D-FGM) having different boundary conditions", Composite Structures, 149, pp. 304–314, 2016. https://doi.org/10.1016/j.compstruct.2016.04.034

[40] Caliò, I., Greco, A., D'Urso, O. "Free vibrations of spatial Timoshenko arches", Journal of Sound and Vibration, 333(19), pp. 4543–4561, 2014. https://doi.org/10.1016/j.jsv.2014.04.019

[41] Kim, G. S., Oh, S. J., Lee, T. E., Lee, B. K. "Free vibrations of axially functionally graded horseshoe arch", Engineering Solid Mechanics, 9(3), pp. 251–262, 2021. https://doi.org/10.5267/j.esm.2021.3.005

[42] Tornabene, F. "Free vibration analysis of functionally graded conical, cylindrical shell and annular plate structures with a four-parameter power-law distribution", Computer Methods in Applied Mechanics and Engineering, 198(37–40), pp. 2911–2935, 2009. https://doi.org/10.1016/j.cma.2009.04.011

[43] Lee, B. K., Wilson, J. F. "Free vibrations of arches with variable curvature", Journal of Sound and Vibration, 136(1), pp. 75–89, 1990. https://doi.org/10.1016/0022-460X(90)90939-W

[44] Borg, S. F., Gennaro, J. J. "Advanced structural analysis", D. Van Nostrand Company, New York, NY, USA, 1959.

[45] Timoshenko, S. P., Goodier, J. N. "Theory of elasticity", McGraw-Hill, 1970. ISBN 9780070858053

[46] Humar, J. L. "Dynamics of structures", Prentice-Hall, 1990. ISBN 978-0132220682

[47] Burden, R. L., Faires, D. J., Burden, A. M. "Numerical analysis", Cengage Learning, 2016. ISBN 9781305253667

[48] Sari, M., Shaat, M., Abdelkefi, A. "Frequency and mode veering phenomena of axially functionally graded non-uniform beams with nonlocal residuals", Composite Structures, 163, pp. 280–292, 2017. https://doi.org/10.1016/j.compstruct.2016.11.093